
Theory and Simulation of Friction and Lubrication

M.H. Müser

Department of Applied Mathematics, University of Western Ontario, London, ON,
Canada N6A 5B7

mmuser@uwo.ca



Martin H. Müser

- 1 Introduction** 67
- 2 Theoretical Background** 68
 - 2.1 Friction Mechanisms 69
 - 2.2 Velocity-Dependence of Friction 72
 - 2.3 Load-Dependence of Friction and Contact Mechanics 74
 - 2.4 Role of Interfacial Symmetry 75
 - 2.5 Common Toy Models 77
- 3 Computational Aspects** 78
 - 3.1 Imposing Load and Shear 78
 - 3.2 Including Surface Roughness and Elastic Deformations 80
 - 3.3 Imposing Constant Temperature 84
 - 3.4 Determination of Bulk Viscosities 89
- 4 Selected Case Studies** 95
 - 4.1 Superlubricity and the Role of Roughness at the Nanometer Scale 95
 - 4.2 Physics and Chemistry of Lubricant Additives 99
- References** 101

Molecular dynamics (MD) and related simulation techniques have proven indispensable in unraveling the microscopic origins of many tribological phenomena such as friction, lubrication, and wear. This chapter is meant to serve as a guide for conducting MD simulations to further deepen our understanding of the processes that occur when two surfaces are in relative sliding motion. Some of the key mechanisms leading to friction will be discussed first. Knowledge of these mechanisms is imperative to both set up and interpret the results of simulations. However, the focus of this chapter will be on technical aspects such as how to construct realistic surface profiles and how to impose load, shear, and temperature during simulations. Finally, a few selected MD studies will be presented.

1 Introduction

Atomistic simulations of friction between solids have received growing attention in the last decade. This increase of interest has been spurred by the miniaturization of mechanical devices, the peculiar behaviour of condensed matter at the nanoscale, and advances in simulating ever more accurately chemically complex lubricants and surfaces [1–3]. Computer simulations have contributed significantly to the identification of dissipation mechanisms and, in some cases, have overthrown previously established explanations of the origin of friction. Despite impressive progress in the field, many open questions of scientific and technological interest persist. To name a few, the microscopic mechanisms leading to sliding-induced wear remain elusive, it is unclear how the interactions between lubricant additives affect lubricant performance and even the friction mechanisms in many relatively well-defined, nano-scale systems have not yet been convincingly identified. This chapter will address these and related issues and point to some unsolved questions. However, the main objective will be to provide guidelines as to how to conduct tribological simulations.¹

Sliding surfaces are generally in a non-equilibrium state. One of the difficulties in simulating materials far away from equilibrium is the lack of a general principle such as minimization of free energy. Along these lines, the equivalence of ensembles in the thermodynamic limit does not apply to many tribological systems. This can be illustrated as follows. In a first simulation of two sliding surfaces, the kinetic friction force, F_k , is determined at constant load and constant sliding velocity. If a consecutive simulation is run in which similar parameters are employed except that now the separation is constrained to d , then one may well obtain completely different values for F_k from the two simulations. This example demonstrates that implementing boundary conditions properly is crucial in non-equilibrium simulations if we want to make

¹ Tribology is the science of surfaces in relative motion. It is sometimes also defined as the science of friction, lubrication, and wear.

reliable predictions. It also illustrates one of many pitfalls that can diminish considerably the value of a largely well-designed tribological simulation. These pitfalls often result from convenience where the unrealistic treatment, in this case constant separation, is easier to implement than the experimental condition, such as constant normal load.

Another important trap to avoid is the use of any artificial symmetries that do not exist in experiments. Unfortunately, it is almost common practice to simulate two identical, perfectly aligned surfaces, which are termed commensurate, although such interfaces are known to behave in a manner that is qualitatively different than that observed when two dislike, or misoriented surfaces, called incommensurate, rub against each other. Neglecting surface curvature or not allowing lubricant to become squeezed out of the contact can also lead to behaviour that would not be found in a regular laboratory experiment. Additionally, temperature control may be a more sensitive issue for systems far from equilibrium than in equilibrium simulations. By imposing shear, we constantly pump energy into the system, which needs to be removed. Thermostating naively may induce unrealistic velocity profiles in the sheared lubricant or lead to other undesired artifacts.

Before discussing the technical aspects of atomistic friction simulations, this chapter will give a small overview of the theoretical background of friction at small velocities. Without such a background, it is difficult to ask meaningful questions and to interpret the outcome of a simulation. After all, our goal goes beyond simply reproducing experimental results. It is often helpful to classify the processes into categories such as linear response, out-of-equilibrium steady state, and strongly irreversible. Moreover, a good understanding of the theoretical background will aid in determining which aspects of the simulations deserve particular focus and which details are essentially irrelevant. In some situations, for example when simulating boundary lubricants exposed to large pressures, the results are typically insensitive to the precise choice of the thermostat, while the opposite holds if the two sliding surfaces are separated by a high Reynold number fluid, or if polymers are grafted onto each surface.

In Sect. 2, some theoretical aspects of friction between solids will be explained. Section 3 contains an overview of algorithms that have been used in the simulation of tribological phenomena, and some selected case studies will be presented in Sect. 4.

2 Theoretical Background

Every-day experience tells us that a finite threshold force, namely the static friction force, F_s , has to be overcome whenever we want to initiate lateral motion of one solid body relative to another. Conversely, when attempting to drag a solid through a fluid medium, there is no such threshold. Instead, one only needs to counteract friction forces linear in the (final) sliding velocity v_0 .

It came as a surprise when Hirano and Shinjo suggested that static friction between solids in ultra-high vacuum may essentially disappear as well [4, 5]. While their suggestion contradicts our intuition, which is based on everyday experience, it does not necessarily contradict Newtonian mechanics. If the slider and substrate have homogeneous surfaces and wear and plastic deformation are negligible, then one may expect the same (free) energy at the beginning of the sliding process as at its end, because of translational invariance. In such a case, no work would have to be done on the system implying the possibility of ultra-low friction, or, in the words by Hirano and Shinjo, superlubricity.

The microscopic justification for the possibility of the virtual absence of lateral forces between solids can be supported by the following argument: There are as many bumps (or atoms) in the substrate pushing the slider to the right as there are surface irregularities pushing it to the left. Hence, statistically speaking, there is the possibility of an almost perfect annihilation of lateral forces. Allowing for long-range, *elastic* deformations does not alter the almost systematic annihilation of lateral forces, unless the systems are extremely soft or extremely rough. Although this is a subject of current research, it appears that this statement remains valid even if one considers surface profiles that would be characteristic of engineering surfaces such as pistons and cylinders in car engines.

In the following, we will discuss why surfaces are usually not superlubric. In general, this is due to energy dissipation through various mechanisms during sliding. The knowledge of the relevant dissipation mechanisms is important when setting up tribological simulations, as it allows one to estimate the validity of the simulations for given laboratory conditions.

2.1 Friction Mechanisms

It has long been realized that solid friction is intimately connected to hysteresis and to what one may call plugging motion. This is best illustrated in the model proposed independently by Prandtl [6] and by Tomlinson [7]. In their model, a surface atom of mass m is coupled to its lattice site via a harmonic spring of stiffness k . The lattice site, which moves at constant velocity v_0 , is assumed to be located in the origin at time $t = 0$. Besides the interaction with its lattice site, the atom experiences a coupling $V_0 \cos(2\pi x/a)$ to the substrate, where V_0 has the unit of energy and reflects the strength of the coupling, a is the lattice constant of the substrate, and x is the current position of the surface atom. Introducing a viscous damping proportional to velocity \dot{x} and damping coefficient γ ,² the surface atom's equation of motion reads

² The damping term can be motivated by the following microscopic picture. When the atom moves very slowly, some lattice vibrations will be induced in the substrate so that energy – or heat – flows away from the interface. The damping term, which may be position dependent, can be calculated in principle from generally

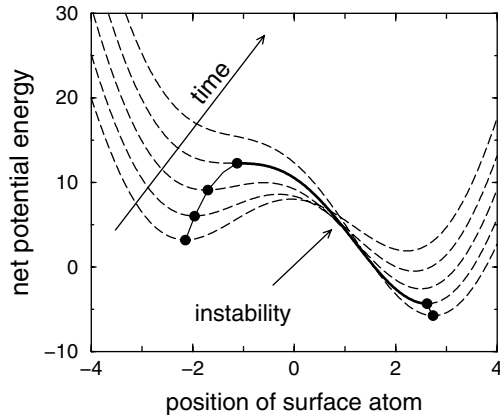


Fig. 1. Illustration of an instability in the Prandtl-Tomlinson model. The sum of the substrate potential and the elastic energy of the spring is shown at various instances in time. The energy difference between the initial and the final point of the thick line will be the dissipated energy when temperature and sliding velocities are very small

$$m\ddot{x} + \gamma\dot{x} = k(v_0t - x) + \frac{2\pi}{a}V_0 \sin(2\pi x/a). \quad (1)$$

If k is very large, i.e., k is greater than the maximum curvature of the potential, $V''_{\max} = (2\pi/a)^2V_0$, then there is always a unique equilibrium position $x_{\text{eq}} \approx v_0t$ for the atom and the atom will always be close to x_{eq} . Consequently, the friction will be linear in v_0 at small values of v_0 .

Things become more interesting once V''_{\max} exceeds k . Now there can and will be more than one stable position at certain instances of time as one can see in Fig. 1. The time dependence of the combined substrate and spring potential reveals that mechanically stable positions disappear at certain instances in time due to the motion of the spring. Consequently, an atom cannot find a mechanically stable position at a time $t + \delta t$ in the vicinity of a position that was stable a small moment δt ago. At times slightly larger than t , the position of the atom becomes *unstable* and, hence, it must move forward quickly towards the next potential energy minimum. After sufficiently many oscillations around the new mechanical equilibrium, most of the potential energy difference between the new and the old equilibrium position is dissipated into the damping term. As a consequence, for sufficiently small v_0 , the dissipated energy per sliding distance is rather independent of v_0 and (in the present example of a bistable system) similarly independent of γ .

Despite its merits, which are further discussed in Sect. 2.5, one should not take the Prandtl-Tomlinson model too literally. There simply is no reason why the inter-bulk coupling, reflected by V''_{\max} , should be stronger than the

valid statistical mechanics arguments by integrating out the substrate's lattice vibrations. A more detailed justification is beyond the scope of this chapter.

intra-bulk coupling k . But even if it were, one would have to expect more dramatic processes than elastic instabilities, such as cold welding and plastic deformation, so that the assumption of an elastic coupling in the slider would break down completely. One could certainly argue that similar instabilities may occur at larger length scales, involving collective degrees of freedom [8]. However, it appears that elastic instabilities do not contribute considerably to dissipation [9]. A notable exception to this rule is rubber, for which sliding friction is related to internal friction rather than to dissipation taking place at the interface [10].

A traditional explanation of solid friction, mainly employed in engineering sciences, is based on plastic deformation [11]. It is assumed that plastic flow occurs at most microscopic points of contact, so that the normal, local pressures correspond to the hardness, σ_h , of the softer of the two opposed materials. The (maximum) shear pressure is given by the yield strength, σ_y , of the same material. The net load, L , and the net shear force, F_s , follow by integrating σ_h and σ_y over the *real* area of contact, A_{real} , respectively, i.e., $L = \sigma_h A_{\text{real}}$ and $F_s = \sigma_y A_{\text{real}}$.³ Hence, the plastic deformation scenario results in the following (static) friction coefficient

$$\mu_s = \sigma_y / \sigma_h , \quad (2)$$

where μ_s is defined as the ratio of F_s and L . Although this explanation for a linear relationship between friction and load has been used extensively in the literature, Bowden and Tabor, who suggested this idea, were aware of the limitations of their model and only meant to apply it to contacts between (bare) metals [11]. There are two important objections to the claim that plastic deformation is generally a dominant friction mechanism. Usually, friction between two solids does not (only) depend on the mechanical properties of the softer of the two opposing materials, but on both materials and the lubricant in the contact. Moreover, theoretical calculations of typical surface profiles have shown that plastic flow should occur at only a very small fraction of the total number of contact points [12].

So far, we have not considered lubricants added intentionally, such as oils, or unintentionally in the form of contaminants, such as short, airborne hydrocarbons. However, such adsorbed molecules alter dramatically the behaviour of sliding contacts, as long as they do not become squeezed out the microscopic points of contact [13, 14]. From an engineering point of view, such molecules keep the two opposed surfaces from making intimate mechanical contact, thereby reducing plastic deformation and wear. However, they also keep surfaces from becoming superlubric. The last one or two layers of lubricant do not become squeezed out of the contact and solidify due to the typically large pressures at the microscopic scale. In this regime, one gener-

³ Intimate mechanical contact between macroscopic solids occurs at isolated points only, typically at a small fraction of the apparent area of contact. The net area of this intimate contact is called the real area of contact A_{real} .

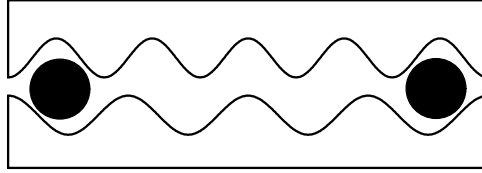


Fig. 2. Schematic representation of the way how adsorbed atoms can lock two non-matching solids. From [14]

ally talks about boundary lubrication. As the interactions between lubricant particles is relatively weak, the adsorbed atoms and molecules will predominantly try to satisfy the interactions with the confining walls. This can lock the surfaces geometrically, as illustrated schematically in Fig. 2. When sliding the top wall relative to the substrate, an energy barrier has to be overcome, generating a static friction force.

There are many other mechanisms leading to dissipation, although they may be less universal than those related to boundary lubricant-induced, geometric frustration. Chemical changes in lubricant molecules, reversible or irreversible, produce heat. Examples are configurational changes in hydrogen-terminated diamond surfaces [16] or terminal groups of alkane chains through isomerization [15] and sliding- and pressure-induced changes in the coordination numbers of surface or lubricant atoms [17, 18]. Although the microscopic details differ significantly, all these examples exhibit a molecular hysteresis similar to the one described in the context of the Prandtl-Tomlinson model. There are also many strongly irreversible tribological phenomena, such as cold-welding, scraping, cutting, or uncontrolled, catastrophic wear. Characterizing them is often tedious, because many of these strongly irreversible processes are system specific and lack a steady state. For these reasons, we will focus mainly on non-equilibrium, steady-state type situations.

It is yet important to realize that simulating strongly irreversible processes often requires more care than those with a well-defined steady state. Most experimental systems are open, while simulations employ confining walls and periodic boundary conditions parallel to the interface. Any debris generated will remain in the interface in the simulations, unless special precaution is taken. One means of simulating open systems is to incorporate lubricant reservoirs, however, this leads to a significant increase in computational effort.

2.2 Velocity-Dependence of Friction

Solid friction is typically relatively independent of the sliding velocity v_0 . This finding, also known as Coulomb's law of friction, [19] can be rationalized nicely in the Prandtl-Tomlinson model. A given number of instabilities occurs per sliding distance, Δx . Each instability will produce a similar amount of heat, ΔQ . In steady state, one may therefore associate the kinetic friction force, F_k , with the quotient

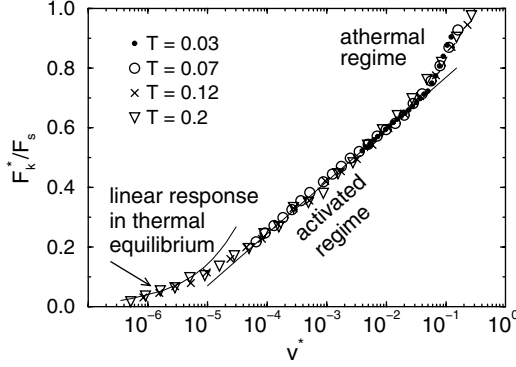


Fig. 3. Typical velocity relationship of kinetic friction for a sliding contact in which friction is due to adsorbed layers confined between two incommensurate walls. The kinetic friction F_k is normalized by the static friction F_s . At extremely small velocities v^* , the confined layer is close to thermal equilibrium and consequently F_k is linear in v^* , as to be expected from linear response theory. In an intermediate velocity regime, the velocity dependence of F_k is logarithmic. Instabilities or “pops” of the atoms can be thermally activated. At large velocities, the surface moves too quickly for thermal effects to play a role. Time-temperature superposition could be applied. All data were scaled to one reference temperature. From [20]

$$F_k = \frac{\Delta Q}{\Delta x}. \quad (3)$$

Once temperature comes into play, the jumps of atoms may be invoked prematurely via thermal fluctuations. Consequently, the spring pulling the surface atom will be less stretched on average. This will decrease the average friction force and render F_k rate or velocity dependent, typically in the following form

$$F_k \approx F_k(v_{\text{ref}}) + c \left(\ln \frac{v_0}{v_{\text{ref}}} \right)^\gamma, \quad (4)$$

where c is a constant, v_{ref} a suitable reference velocity, and γ an exponent in the order of unity. Of course, this equation will only be valid over a limited velocity range. In many cases, F_k becomes linear in v_0 at very small values of v_0 , i.e., when one enters the linear response regime, in which the system is always close to thermal equilibrium.

An example for the velocity dependence of friction is given in Fig. 3 for a boundary lubricant confined between two incommensurate surfaces [20]. For the given choice of normal pressure and temperature, one finds four decades in sliding velocity, for which (4) provides a reasonably accurate description. In the present case, c is positive and the exponent γ is unity. Neither of the two statements is universal. For example, the Prandtl-Tomlinson model can best be described with $\gamma = 2/3$ in certain regimes, [21,22] while confined boundary lubricants are best fit with $\gamma = 1$ [20,23]. Moreover, the constant c can become negative, in particular when junction growth is important. The local contact

areas can grow with time due to slow plastic flow of the opposed solids or due to adhesive interactions mediated by water capillaries, which increase in time [8, 24, 25].

2.3 Load-Dependence of Friction and Contact Mechanics

Many macroscopic systems show an almost linear relationship between (static) friction, F_s , and load, L ,

$$F_s = \mu_s L, \quad (5)$$

where the (static) friction coefficient, μ_s , does not depend on the apparent area of contact. The origin of this linear dependence, which is also called Amontons' law, is subject to controversy.

One explanation of Amontons' law is based on microscopic arguments. It had been argued by Bowden and Tabor [11] that the following constitutive relation for shear stress σ_s and normal stress σ_n holds microscopically

$$\sigma_s = \sigma_0 + \alpha \sigma_n \quad (6)$$

for many systems, where σ_0 and α are constant. From this one obtains $F_s = \sigma_0 A_{\text{real}} + \alpha L$, so that one may associate α as the (differential) friction coefficient provided that σ_0 is sufficiently small. Simulations of boundary lubricants for systems with flat surfaces suggest that (6) may often be reasonably accurate up to pressures close to the yield strength of solids and that the term related to σ_0 are indeed often negligible [13, 26].

The reason for the linearity of shear and normal pressures can be rationalized qualitatively by considering Fig. 2. In order for the top wall to move to the right it must move up a slope, which is dependent upon how the adsorbed atom is interlocked between the substrate and the slider.

Of course, this argument is highly qualitative, because it assumes implicitly that non-bonded atoms behave similar to hard disks in areas of high pressure. Moreover, this argument must be modified if curved surfaces are considered [27]. However, it appears to be a reasonable approximation for many systems.

Another scenario leading to Amontons' law is related to the macroscopic contact mechanics. Even highly polished surfaces are rough on many different length scales. A way of characterizing roughness is to average or measure the height difference auto-correlation function $C_2(\Delta r)$

$$C_2(\Delta r) = \langle [h(\mathbf{r}) - h(\mathbf{r} + \Delta \mathbf{r})]^2 \rangle, \quad (7)$$

over one or several statistically identical samples, where $h(\mathbf{r})$ is the height of a sample's surface at the position $\mathbf{r} = (x, y)$. Thus, $C_2(\Delta r)$ states what variation in height we expect if we move away a distance Δr from our current position. For many real surfaces, power law behaviour according to

$$C_2(\Delta r) \propto \Delta r^{2H}, \quad (8)$$

is found, where H is called the Hurst roughness exponent. $H = 1/2$ would correspond to a random walk in the height as we move laterally over the surface. Surfaces satisfying 8 are called self-similar. Ways of constructing self-similar surfaces for simulations will be described in Sect. 3.2.

When two macroscopic solids with fractal surfaces are brought into contact, only a small fraction of the surfaces, the so-called real area of contact, A_{real} , will be in microscopic, mechanical contact. It can be shown that the pressure distribution averaged over these real contacts is surprisingly independent of the externally imposed load, L , provided that the surfaces are not too adhesive or too compliant [12, 28, 29]. This implies that Amontons' law can also result from macroscopic contact mechanics irrespective of the local relation between normal and shear pressure. However, when conditions are less ideal and adhesion and plastic deformation are starting to play a role, the independence of the pressure distribution on the net load is not valid any longer [30]. Hence, different scenarios can lead to the observation of Amontons' law depending on the details of the system of interest.

2.4 Role of Interfacial Symmetry

Imagine two egg cartons placed on top of each other. If you try to move the top carton by applying a lateral force, you will have to pull harder if the cartons are oriented than if they are brought out of registry. If the two cartons are separated by eggs, there still will be a tremendous influence of the orientation on the required lateral force to slide the cartons. The same notion holds for surfaces that are separated by confined atoms and molecules. Commensurate surfaces, i.e., those that are identical and perfectly aligned, will have the tendency to have much larger (static) friction than those that are misoriented or dislike. Therefore, whenever we impose symmetries into our systems, we risk observing behaviour that is inconsistent with observed when these symmetries are absent. Since opposing surfaces are essentially always dislike, unless they are prepared specifically, it will be important to avoid symmetries in simulations as much as possible.

It may come as a surprise to some that two commensurate surfaces can withstand finite shear strength even if they are separated by a fluid [31]. But one has to keep in mind that breaking translational invariance automatically induces a potential of mean force \mathcal{F} . This is why metals, which are mainly glued together through “fluid-like” conduction electrons, have finite shear moduli. Due to the symmetry breaking, commensurate walls can be pinned even by an ideal gas embedded between them [32]. The reason is that \mathcal{F} scales linearly with the area of contact. In the thermodynamic limit the energy barrier for the slider to move by one lattice constant becomes infinitely high so that the motion cannot be thermally activated and, hence, static friction becomes finite. No such argument applies when the surfaces do not share a common period.

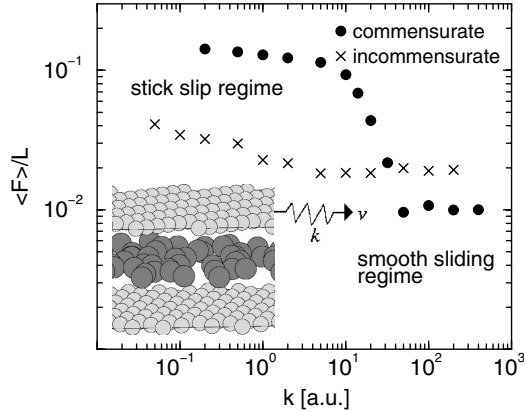


Fig. 4. Kinetic friction F_k as a function of the stiffness k of the spring pulling the upper wall at constant, small velocity. The inset shows a part of the simulated system. At large values of k , the slider moves at the same velocity as the spring and the smooth sliding kinetic friction is probed. At small values of k , the system manages to lock into a potential energy minimum, similar to what happens in the Prandtl-Tomlinson model. The surface then undergoes plugging or “stick-slip” motion as a whole. In that regime, the measured friction approaches the value for static friction. Commensurability affects the measured values for F_k in both regimes sensitively. From [20]

Not only static friction, F_s , but also kinetic friction, F_k , is affected by commensurability. If two crystalline surfaces are separated by one atomic layer only, F_k may actually be reduced due to commensurability, although static friction is increased [20]. The strikingly different behaviour for commensurate and incommensurate systems is demonstrated in Fig. 4.

Unfortunately, it can be difficult to make two surfaces incommensurate in simulations; particularly when two identical, crystalline surfaces are slid against each other. The reason is that only a limited number of geometries conform to the periodic boundary conditions in the lateral direction. Each geometry needs to be analyzed separately and there is little general guidance one can give. For surfaces with trigonal symmetry, such as [111] surfaces of face-centered cubic crystals, it is often convenient to rotate the top wall by 90° . This rotation does not map the trigonal lattice onto itself. The numbers of unit cells in x and y direction should be chosen such that they need to be strained only marginally to form an interface with a square geometry. The top view of some incommensurate structures between trigonal surfaces is shown in Fig. 5. In most cases, the measured friction between incommensurate walls is relatively insensitive to how incommensurability is achieved, as long as the roughness of the two opposing walls remains constant [14].

Typical surfaces are usually not crystalline but have amorphous layers on top. These amorphous walls are much rougher at the atomic scale than

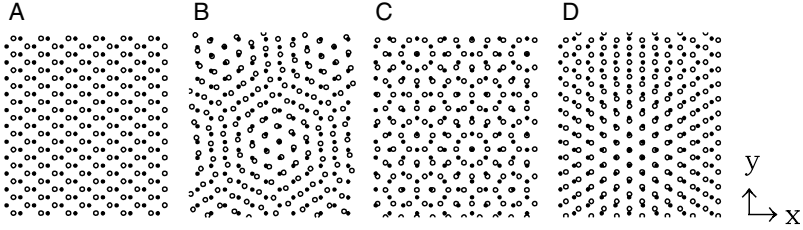


Fig. 5. Projections of atoms from the bottom (*solid circles*) and top (*open circles*) surfaces into the plane of the walls. (A through C) The two walls have the same structure and lattice constant, but the top wall has been rotated by 0° , 11.6° , or 90° , respectively. (D) The walls are aligned, but the lattice constant of the top wall has been reduced by $12/13$. The atoms can only achieve perfect registry in the commensurate case (A). From [13]

the model crystalline surfaces, which one prefers to use for computational convenience and for fundamental research. The additional roughness at the microscopic level due to disorder increases the friction between surfaces considerably even when they are separated by a boundary lubricant [14]. However, no studies have been done to explore the effect of roughness on boundary-lubricated systems systematically and only a few attempts have been made to investigate dissipation mechanisms in the amorphous layers under sliding conditions from an atomistic point of view.

2.5 Common Toy Models

The Prandtl-Tomlinson model introduced in Sect. 2.1 is the most commonly used toy model for simulations of frictional phenomena. It has a tremendous didactic value, because it shows nicely the important role of instabilities. Moreover, it is used frequently to describe quite accurately the dynamics of an atomic force microscope tip that is dragged over a periodic substrate [33]. It is worthwhile to run a few simulations of the Prandtl-Tomlinson model and to explore its rich behaviour. In particular, interesting dynamics occurs when k is sufficiently small such that the surface atom is not only bistable but multistable and γ is so small that the motion is underdamped. In such a situation, the atoms do not necessarily become arrested in the next available, mechanically stable site after after depinning and interesting non-linear dynamics can occur, such as non-monotonic friction-velocity dependence.

Another frequently-used model system is the Frenkel Kontorova (FK) model, in which a linear harmonic chain is embedded in an external potential. For a review we refer to [34]. The potential energy in the FK model reads

$$V = \sum_i \left\{ \frac{1}{2} k (x_{i+1} - b - x_i)^2 - V_0 \cos(2\pi x_i/a) \right\}, \quad (9)$$

where a and b are the lattice constant of substrate and slider respectively, and k is the strength of the spring connecting two adjacent atoms in the slider. As in the Prandtl Tomlinson model, finite friction is found when atoms can find more than one mechanically meta-stable position and become unstable during sliding. Experience indicates that it is not possible to reproduce tribological experimental results with the FK model despite the increase in complexity with respect to the model of Prandtl and Tomlinson. This calls into question the use of the FK model when interpreting experimental results. In particular, when parametrized realistically and generalized to higher dimensions, it is found that most incommensurate interfaces between crystals should be superlubric within the approximations of the FK model [5]. Otherwise, when instabilities do occur, the FK model can only describe the early time behaviour of flat sliding interfaces [35]. Conversely, in other contexts, such as the motion of charge density waves, pinning and dissipation may be realistically described by the FK model.

3 Computational Aspects

Simulating solids in relative motion may require considerations additional to those needed for equilibrium simulations of bulk phases. Shear and load need to be imposed in a way that mimics experimental setups. Surfaces have to be defined and often it is important to include their deformation in the simulation accurately, which we want to do at a small computational expense. Heat needs to be removed, which requires us to know the properties of thermostats. This chapter will be concerned with these and related aspects.

3.1 Imposing Load and Shear

In many simulations of tribological phenomena, two opposed solids are separated by a lubricating film. A sketch is shown in Fig. 6. It is natural to subdivide the system into a substrate, a slider, and the remaining system. Sometimes, one may only be interested in the bulk properties of a lubricant under shear or under extreme pressure conditions, in which case, there is no need to introduce surfaces, see the discussion in Sect. 3.4. Otherwise, when walls are included, it is certainly desirable to keep the interface as unperturbed as possible from any external mechanical forces. This is why it is good practice to only couple the outermost layers of the substrate and slider to constraints, external forces, and thermostats. In the following, the term bottom layer will be used to specify the outermost layer of the substrate and top layer will stand for the outermost layer of the slider, although one may certainly choose more than one single layer to be part of it. All explicitly simulated atoms that are not part of the outermost layers will be referred to as the embedded system, even if they belong to the confining walls.

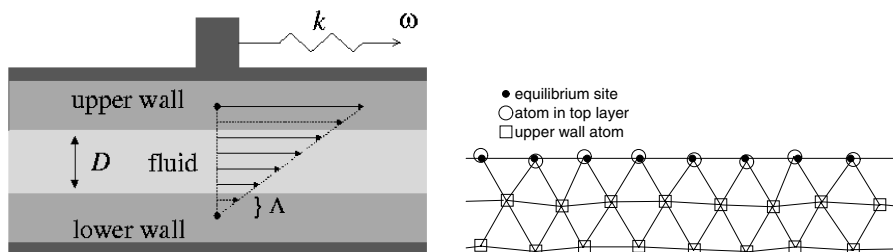


Fig. 6. *Left:* Schematic graph of the set-up for the simulation of rubbing surfaces. Upper and lower walls are separated by a fluid or a boundary lubricant of thickness D . The outermost layers of the walls, represented by dark color, are often treated as rigid unit. The bottom most layer is fixed in laboratory system and the upper most layer is driven externally, for instance by a spring of stiffness k . Also shown is a typical, linear velocity profile for a confined fluid with finite velocities at the boundary. The length at which the fluid's drift velocity would extrapolate to the wall's velocity is called the slip length λ . *Right:* The top wall atoms in the rigid top layer are set onto their equilibrium sites or coupled elastically to them. The remaining top wall atoms interact through interatomic potentials, which certainly may be chosen to be elastic

By convention, we will keep the center of mass of the bottom layer fixed and couple the top layer to an external driving device. There are three commonly used modes under which top layers are driven:

1. Predefined trajectory, e.g., $X = X(t)$
2. Predefined force, e.g., $F = F(t)$
3. Pulling with a spring, e.g., $F_x = -k[X - X_0(t)]$, where F_x would be the force acting on the top layer in x direction, k would reflect the (effective) stiffness of the driving device, and $X_0(t)$ denotes the position of the driving device as a function of time.

The typical choices for the predefined trajectories or forces are constant velocity, including zero velocity, constant separation, and constant forces and/or oscillatory velocities and forces. It is certainly possible to drive different Cartesian coordinates with different modes, e.g., to employ a constant force or load perpendicular to the interface and to use a predefined velocity, constant or oscillatory, parallel to a direction that has no component normal to the interface. Mimicking experiments done with a tribometer would typically best be done in constant velocity or constant force modes, whereas rheometers usually employ oscillatory motion in lateral direction.

Note that pulling a point particle over a periodic potential in mode (3) resembles the Prandtl-Tomlinson model discussed in the previous section. As is the case for the Prandtl Tomlinson model, the result for the (kinetic) friction force can depend sensitively on the stiffness of the driving spring, see also Fig. 4. Weak springs tend to produce higher friction than soft springs. This can be important to keep in mind when comparing simulations to experiments.

The measured friction is not only a function of the interface but also of how the interface is driven.

It is often beneficial to define a coordinate \mathbf{R}_{tl} that describes the center of mass of the top layer. There are three common ways how to set up the top layer. (i) To confine the position of top layer atoms \mathbf{r}_n to (lattice) sites $\mathbf{r}_{n,0}$, which are connected rigidly to the top layer. (ii) To couple the top layer atoms elastically to sites $\mathbf{r}_{n,0}$ fixed relative to the top layer, e.g., with springs of stiffness k . (iii) To employ an effective potential, such as a Steele potential, V_S , [36] between embedded (em) atoms and top layer. There are specific advantages and disadvantages associated with each method. Approach (i) may be the one that is most easily coded, (ii) allows one to thermostat effectively the outermost layer, while (iii) is probably cheapest in terms of CPU time.

Depending on the choice of the interaction between the top layer and the embedded system, the force on the top wall, \mathbf{F}_{tl} , needs to be evaluated differently.

$$\mathbf{F}_{\text{tl}} = \mathbf{F}_{\text{ext}} + \begin{cases} \sum_{n \in \text{tl}} \mathbf{f}_n & \text{(i)} \\ \sum_{n \in \text{tl}} -k(\mathbf{r}_n - \mathbf{r}_{n,0}) & \text{(ii)} \\ \sum_{n \in \text{em}} -\nabla_n V_S(\mathbf{r}_n) & \text{(iii)} \end{cases}, \quad (10)$$

where \mathbf{f}_n in line (i) denotes the force on atom n and $\nabla_n V_S$ is the gradient of the surface potential with respect to an embedded atom's position. \mathbf{F}_{tl} will be used to calculate the acceleration of the top layer, resulting in a displacement $\Delta \mathbf{R}_{\text{tl}}$. This displacement needs to be added to the sites $\mathbf{r}_{n,0}$ contained in the top layer in cases (i) and (ii).

It is certainly possible to choose the mass M_{tl} of the top layer arbitrarily. For example, one may have M_{tl} incorporate some mass of the top wall that is not explicitly included in the simulation. However, when doing this, one needs to be aware of two effects. First, the time scale gap between the fast atomic motion and the slow collective motion of the confining wall. However, having the top wall move on shorter time scales than in real systems may help to overcome the time scale gap between simulations and experiments. Second, the measured friction may depend on the mass of the top wall when it is pulled with a spring. Large masses favor smooth sliding over stick-slip motion and hence reduce the measured friction [37, 38]. In general, it turns out to be very difficult to deduce information on the embedded system from tribological or rheological experiments without considering carefully the properties and the driving of the external system [39].

3.2 Including Surface Roughness and Elastic Deformations

Surface Geometries

Crystalline surfaces are often employed both experimentally and in simulations, when studying friction from a fundamental point of view. It is a relatively straightforward procedure to set up crystalline surfaces, which is why

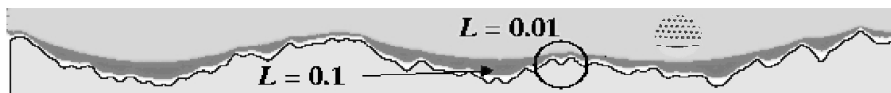


Fig. 7. Flat elastic manifold pressed against a self-affine rigid surface for different loads L per atom in top wall. The inset shows some atomic-scale details of the contact

we will not comment on them in any more detail. However, as mentioned in Sect. 2.3, many (engineering) surfaces are self similar over several length scales. A profile of a self-similar surface geometry is shown in Fig. 7 together with a flat elastic object pressed onto the rough substrate. In the recent past, there has been an intensified interest in modeling more realistically surface profiles, however, so far the research has focused on contact mechanics rather than on sliding motion between fractal surfaces [12, 28, 29].

There are various ways of constructing self-affine surfaces [40]. Some of them do not allow one to produce different realizations of surface profiles, for example by making use of the Weierstrass function. Such methods should be avoided in the present context, because it would be hard to make statistically meaningful statements without averaging over a set of statistically independent realizations. An appropriate method through which to construct self-similar surfaces is to use a representation of the height profile $h(x)$ via its Fourier transforms $\tilde{h}(q)$.

In reciprocal space, the self-affine surfaces described in (7) and (8) are typically characterized by the spectrum $\tilde{S}(q)$ defined as

$$\tilde{S}(q) = \langle \tilde{h}(q)\tilde{h}^*(q) \rangle, \quad (11)$$

with

$$\begin{aligned} \langle \tilde{h}(q) \rangle &= 0 \\ \langle \tilde{h}(q)\tilde{h}^*(q') \rangle &\propto q^{-2H-d}\delta(q-q'), \end{aligned} \quad (12)$$

where d is the number of independent coordinates on which the height depends, i.e., $d = 1$ if $h = h(x)$, and $d = 2$ if $h = h(x, y)$. $\tilde{S}(q)$ is the Fourier transform of the height autocorrelation function $S(\Delta x) = \langle h(x)h(x + \Delta x) \rangle$. The height-difference autocorrelation function $C_2(\Delta x)$ and $S(\Delta x)$ are related through $2S(\Delta x) = C_2(0) - C_2(\Delta x)$.

In principle, to fully characterize the stochastic properties of surfaces, higher-order correlations of the height function have to be incorporated. However, doing this is tedious computationally and, in most cases, will probably not change significantly the results of the simulation.

One approach to the generation of height profiles is to draw (Gaussian) random numbers for the real and complex parts of $\tilde{h}(q)$ with a mean zero and defined variance and to divide the random number by a term proportional to $q^{H+d/2}$, so that (12) is satisfied. Furthermore, $\tilde{h}(-q)$ must be chosen to be the complex conjugate to ensure that $h(x)$ is a real-valued function.

Alternatively, one may simply write $h(x)$ as a sum over terms $h(q) \cos(qx + \varphi_q)$. In this case, one needs to draw one (Gaussian) random number with the proper second moment of $h(q)$ with zero mean and one random number for each phase φ_q , which is uniformly distributed between 0 and 2π and filter the absolute value of $h(x)$ in the same way as described in the previous paragraph. There are also other techniques which allow one to generate fractal surfaces. One of them is the so-called midpoint algorithm, described in [30].

Multiscale Approaches

It is certainly desirable to simulate as many layers of the confining walls as possible, in order to closely reproduce experimental situations. However, from a computational point of view, one would like to simulate as few degrees of freedom as possible. Unless conditions are special, all processes far away from the interface can be described quite accurately within elastic theory or other methods that allow for a description of plastic deformations, such as finite elements. The advantage of these continuum-theory based methods is that it is possible to coarse-grain the system increasingly as one moves away from the interface, thereby reducing the computational effort. New methodological developments even allow one to couple atomistic simulations to continuum-theory descriptions [41, 42]. It would be out of the scope of this chapter to provide a detailed description, however, the coordination discretisation scheme shown in Fig. 8 alludes to how one must proceed when incorporating different mesh sizes into a simulation.

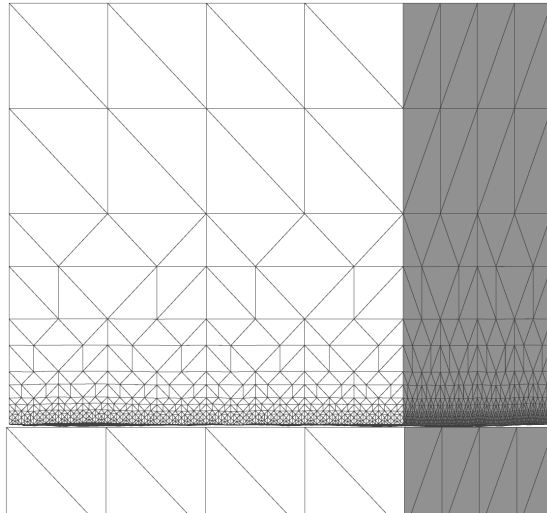


Fig. 8. Representation of a finite-element mesh for the simulation between a fractal, elastic object and a flat substrate. From [12]

While quasi-static processes can be modeled quite well with continuum-mechanics based models employing varying mesh size, this is not the case for dynamic processes. Whenever there is a region where the coarse-grain level is changed, one risks to introduce artificial dynamics. In particular, the transmission of sound waves and energy density is suppressed whenever the mesh size changes. It is not possible to have the proper momentum and energy transfer across the boundary when employing a Hamiltonian-based description. It is important, however, to realize that the computational effort required to simulate a three-dimensional system of linear dimension L only scales with $L^2 \ln L$ using coarse-grained models, as opposed to the L^3 scaling for brute-force methods. It is often advisable to sacrifice realistic dynamics rather than system size.

An alternative method would be to integrate out the elastic degrees of freedom located above the layer that we chose to be the top layer in our simulation [43]. The elimination of the degrees of freedom can be done within the context of Kubo theory, or more precise Zwanzig formalism, leading to effective (potentially time-dependent) interactions between the atoms in the top layer [44, 45]. These effective interactions include those mediated by the degrees of freedom, which have been integrated out. For periodic solids, a description in reciprocal space decouples different wave vectors, q , at least as far as the *static* properties are concerned. This in turn implies that the computational effort also remains in the order of $L^2 \ln L$, provided that use is made of the fast Fourier transform for the transformation between real and reciprocal space. The description is exact for purely harmonic solids, so that one can mimic the static contact mechanics between a purely elastic lattice and a substrate with one single layer only.

There is even the possibility of including *dynamical* effects in terms of time-dependent friction terms (plus random forces at finite temperatures) [44, 45]. However, it may not be advisable to take advantage of this possibility, as the simulation would become increasingly slow with increasing number of time steps. Moreover, the simulation will slow down considerably in higher dimensions due to the non-orthogonality of the dynamical coupling in reciprocal space.

To be specific regarding the formalism, let $\tilde{u}_{qi\alpha}(t)$ denote the α component of the displacement field associated with wave vector q and eigenmode i at time t .⁴ In the absence of external forces, which can simply be added to the equation, the equation of motion for the coordinates that are not thermostated explicitly, $\tilde{u}_{qi\alpha}$, would read:

$$M\ddot{\tilde{u}}_{qi\alpha}(t) = -G_{qi}u_{qi\alpha}(t) + \int_{-\infty}^t dt' \sum_{q',j} \sum_{\beta=1}^3 \gamma_{q'i\alpha}^{q'j\beta}(t-t') \dot{u}_{q'j\beta}(t') + \Gamma_{qi\alpha}(t), \quad (13)$$

⁴ At this point, all interactions within the top plate and above it have already been integrated out. The $\tilde{u}_{qi\alpha}$ are only eigenmodes within this reduced or effective description but not of the full semi-infinite solid.

where the G_{qi} are the (static) Green's functions, or effective spring constants, associated with eigenmode i and wavelength q . The knowledge of these functions enables us to work out the static contact mechanics. The time-dependent damping coefficients $\gamma_{q i \alpha}^{q' j \beta}(t - t')$ in (13) reflect the dynamical coupling between various eigenmodes. There is no reason why this coupling should be diagonal in any of its indices and thus, including the terms related to dynamics, increases memory requirements and slows down the speed of the calculation tremendously, i.e., beyond the expense of approximating a semi-infinite solid by a discrete, elastic lattice of size L^3 . Included in (13) are random forces $\Gamma_{q i \alpha}(t)$, which must be used at finite temperature to counterbalance the time-dependent damping term. The random and damping terms have to be chosen such that they satisfy the fluctuation-dissipation theorem [46].

3.3 Imposing Constant Temperature

The external driving imposed on solids leads to dissipation of energy or heat. In experiments, this heat diffuses away from the interface into the bulk and eventually into the experimental apparatus. In simulations, system sizes are rather limited which makes it necessary to remove heat artificially if one wants to control temperature. Ideally, this is done by thermostating the outermost layers only. Sometimes, however, there are no confining walls, for example in simulations of bulk fluids, or for some reason, the confining walls are better kept rigid. In these cases, the thermostat needs to be applied to the sheared system directly.

There are numerous ways of thermostating systems that are in equilibrium, each with its specific advantages and disadvantages. For situations in which the system is far from equilibrium, stochastic thermostats have proven particularly beneficial, Langevin thermostats being the prototype, [47] and dissipative particle dynamics (DPD) being a modern variation thereof [48]. While stochastic thermostats can be motivated in principle from linear response theory, i.e., there are rigorous schemes for the derivation of the damping terms and the fluctuation terms contained in stochastic thermostats [46]. We will not provide these arguments here and instead focus on their implementation and properties.

Langevin Thermostat

In the Langevin description, one assumes that the degrees of freedom that are not explicitly taken into account, exert, on average, a damping force linear in velocity, $\gamma_i \dot{\mathbf{r}}_i$, as well as additional random forces $\Gamma_i(t)$. This leads to the following equation of motion for particle number i :

$$m_i \ddot{\mathbf{r}}_i + \gamma_i (\dot{\mathbf{r}}_i - \langle \mathbf{v}_i \rangle) = -\nabla_i V + \Gamma_i(t) , \quad (14)$$

where the damping coefficient γ_i and the α component of the random forces $\Gamma_{i\alpha}(t)$ acting on particle i should obey

$$\begin{aligned}
\langle \Gamma_{i\alpha}(t) \rangle &= 0 \\
\langle \Gamma_{i\alpha}(t) \Gamma_{j\beta}(t') \rangle &= 2\gamma_i k_B T \delta(t-t') \delta_{ij} \delta_{\alpha\beta} \\
&\rightarrow 2\gamma_i k_B T \frac{1}{\Delta t} \delta_{t,t'} \delta_{ij} \delta_{\alpha\beta}, \tag{15}
\end{aligned}$$

in order to satisfy the fluctuation-dissipation theorem. In (14), V denotes the total potential energy and $\langle \mathbf{v}_i \rangle$ the expected drift velocity, [49] e.g., $\langle \mathbf{v}_i \rangle = 0$ in the bottom layer and $\langle \mathbf{v}_i \rangle = \mathbf{v}_{tl}$ if atom i belongs to the top layer. The last line in (15) refers to the discrete time description used in molecular dynamics in which Δt is the time step. When using predictor-corrector methods (velocity Verlet is a second-order Gear predictor corrector method), it is necessary to keep in mind that random terms cannot be predicted. Therefore, one should only apply the predictor-corrector schemes to the deterministic parts of the equation of motion. In those cases, where very high damping is employed, time steps can be kept large when employing efficient integration schemes [52]. In general, however, one should keep thermostating sufficiently weak as to avoid externally imposed overdamping.

It also needs to be emphasized that there is no need to chose the random forces from a Gaussian distribution, unless one is interested in short-time dynamics. It is much faster to generate uniformly distributed random numbers for the $\Gamma_i(t)$'s on an interval $[-\sqrt{3}\sigma, \sqrt{3}\sigma]$, where σ is the standard deviation of the Gaussian distribution. Moreover, having a strict upper bound in the $\Gamma_i(t)$'s eliminates potentially bad surprises when using higher-order predictor corrector schemes and, thus, allows one to use a large time step while producing accurate thermal averages and trajectories.

It is certainly also possible to make damping and, hence, thermostating direction dependent, for example, by suppressing the damping terms parallel to the sliding direction. This is particularly important when the system has a small viscosity or when the shear rates are high, because one is likely to create artificial dynamics otherwise. Using the correct velocity profile $\langle \mathbf{v} \rangle$ prior to the simulation can also reduce the problem of perturbing the dynamics in an undesirably strong fashion. However, anticipating certain velocity profiles will always suppress other modes, e.g., assuming laminar flow in a thermostat is likely to artificially bias towards laminar flow [53] and may create additional artifacts [54–56].

Effects of Damping on Calculated Friction

Making assumptions on how heat is dissipated can also influence solid friction, although typically it is less of an issue. This can be most easily explored within the Prandtl Tomlinson model. The lessons to be learned apply to a large degree to more general circumstances. In the original formulation, see (1), damping takes place relative to the substrate. However, one may also assume that the conversion of energy into heat takes place within the top solid [57]. Thus a generalized Prandtl-Tomlinson model would be

$$m\ddot{x} + \gamma_{\text{sub}}\dot{x} + \gamma_{\text{top}}(\dot{x} - v_0) = -\nabla V - k(x - v_0t) + \Gamma_{\text{sub}}(t) + \Gamma_{\text{top}}(t), \quad (16)$$

where the indices “sub” and “top” denote the thermal coupling to substrate and top solid respectively.

To investigate the way in which the thermostat affects frictional forces, it is instructive to study slightly underdamped or slightly overdamped motion. In the following, we will set $m = 1$, $a = 1$, $V_0 = 1$, $k = 0.5 V''_{\text{max}}$. Damping, γ , and temperature, T , will be varied, but we will first consider the athermal case $T = 0$. With this choice of parameters, the maximum curvature of the potential, V''_{max} , will be greater than k so that instabilities will occur under sliding leading to finite kinetic friction at small v_0 in the absence of thermal fluctuations. Figure 9(a) shows the friction-velocity dependence for the following choices of thermostats (i) $\gamma_s = 1$, $\gamma_t = 0$, (ii) $\gamma_s = 0$, $\gamma_t = 1/4$, (iii) $\gamma_s = 0$, $\gamma_t = 1$, (iv) $\gamma_s = 0$, $\gamma_t = 4$.

We see that the kinetic friction is rather insensitive to the precise choice of the thermostat for small values of v_0 , at least as long as the temperature is sufficiently small. This is because friction is dominated by fast “pops” in that regime. This conclusion becomes invalid only if γ is sufficiently small such that a/v_0 , the time it takes the driving stage to move by one lattice constant, is not long enough to transfer most of the “heat” produced during the last instability into the thermostat. At high velocities, the sliding velocity v_0 is no longer negligible when compared to the peak velocity during the instability. This renders the friction-velocity dependence susceptible to the choice of the thermostat. Damping with respect to the substrate leads to strictly monotonically increasing friction forces, while damping with respect to the top wall can result in non-monotonic friction-velocity relationships.

So far, we have considered the zero temperature case. Once finite thermal fluctuations are allowed, there is a qualitatively different friction-velocity relationship, which can be shown by choosing thermal energies as small as $k_B T = 0.1V_0$, see Fig. 9(b). Jumps can now be thermally activated and the friction force decreases with decreasing velocity. Yet again, at small v_0 there is little effect of the thermostat on the measured friction forces. Changing γ_t by as much as a factor of 16 results in an almost undetectable effect at small v_0 . At very small sliding velocities, v_0 , the system can get very close to thermal equilibrium at every position of the top wall, which is why linear response theory is applicable in that regime. It then follows that friction and velocity are linear at sufficiently small values of v_0 . This is generally valid unless the energy barriers to sliding are infinitely high, which explains the linear dependence of friction upon the velocity at small v_0 and finite T , as shown in Fig. 3.

Dissipative-Particle-Dynamics Thermostat

A disadvantage of Langevin thermostats is that they require a (local) reference system. Dissipative particle dynamics (DPD) overcomes that problem by

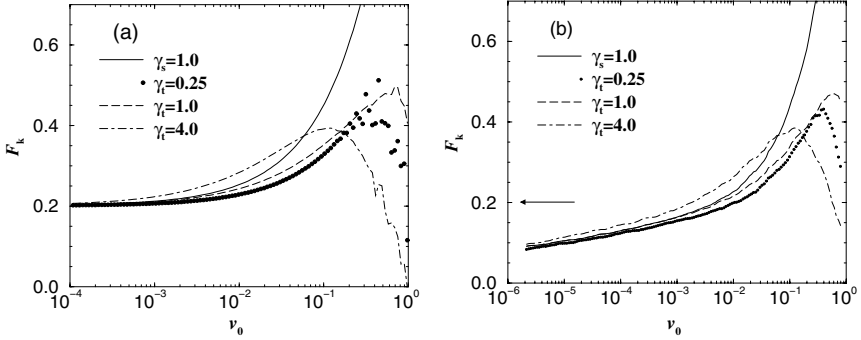


Fig. 9. Friction velocity relationship $F_k(v_0)$ in the Prandtl Tomlinson model at (a) zero and (b) finite thermal energy, i.e., $k_B T = 0.1 V_0$. Different damping with respect to substrate γ_s and top solid γ_t for different realizations of damping. The arrow in (b) points to the zero-velocity limit in the athermal case

assuming damping and random forces in the center-of-mass system of a pair of atoms. The DPD equations of motion read

$$m\ddot{\mathbf{r}}_i = -\nabla_i V - \sum_j \gamma_{ij}(\dot{\mathbf{r}}_i - \dot{\mathbf{r}}_j) + \mathbf{F}_{ij}(t), \quad (17)$$

where $\mathbf{F}_{ij}(t) = -\mathbf{F}_{ji}(t)$. The usual relations for fluctuation and dissipation apply

$$\langle \mathbf{F}_{ij,\alpha}(t) \rangle = 0 \quad (18)$$

$$\langle \mathbf{F}_{ij,\alpha}(t) \mathbf{F}_{kl,\beta}(t') \rangle = 2k_B T \gamma_{ij} (\delta_{ik} \delta_{jl} + \delta_{il} \delta_{jk}) \delta_{\alpha\beta} \frac{\delta_{t,t'}}{\Delta t} \quad (19)$$

Note that γ_{ij} can be chosen to be distance dependent. A common method is to assume that γ_{ij} is a constant for a distance smaller than a cut-off radius $r_{\text{cut,DPD}}$ and to set $\gamma_{ij} = 0$ otherwise. Since calculating random numbers may become a relatively significant effort in force-field based molecular dynamics, it may be sensible to make $r_{\text{cut,DPD}}$ smaller than the cut-off radius for the interaction between the particles, or to have the thermostat act only every few time steps.

Among the advantages of DPD over Langevin dynamics are conservation of momentum and the ability to describe hydrodynamic interactions with longer wavelengths properly, [50, 51] ensuring that “macroscopic” properties are less effected with DPD than with Langevin dynamics. To see this, it is instructive to study the effect that DPD and Langevin have on a one-dimensional, linear harmonic chain with nearest neighbor coupling, which is the simplest model to study long wave length vibrations.

The Lagrange function L of an unthermostated harmonic chain is given by

$$L = \sum_{i=1}^N \frac{m}{2} \dot{x}_i^2 - \frac{k}{2} (x_i - x_{i-1} - a)^2, \quad (20)$$

where a is the lattice constant, k the stiffness of the springs. Periodic boundary conditions are employed after a distance Na . The equations of motion at zero temperature with damping are

$$m\ddot{x}_i + \gamma\dot{x}_i = -k(2x_i - x_{i+1} - x_{i-1}) \quad (\text{Langevin}) \quad (21)$$

$$m\ddot{x}_i + \gamma(2\dot{x}_i - \dot{x}_{i+1} - \dot{x}_{i-1}) = -k(2x_i - x_{i+1} - x_{i-1}) \quad (\text{DPD}) \quad (22)$$

As usual it is possible to diagonalize these equations of motion by transforming them into reciprocal space. The equations of motion of the Fourier transforms $\tilde{x}(q, \omega)$ then read

$$-m\omega^2\tilde{x} + im\omega\gamma\tilde{x} + 4\sin^2(qa/2)k\tilde{x} = 0 \quad (\text{Langevin}) \quad (23)$$

$$-m\omega^2\tilde{x} + 4\sin^2(qa/2)im\omega\gamma\tilde{x} + 4\sin^2(qa/2)k\tilde{x} = 0 \quad (\text{DPD}). \quad (24)$$

Thus while Langevin and DPD damping do not alter the eigenfrequencies of the chain, i.e., their q dependence is, $\omega_0(q) = \sqrt{4\sin^2(qa/2)/m}$, the quality factor Q , defined as the ratio of eigenfrequency and damping, does differ between the two methods,

$$Q(q) = \frac{\omega_0(q)}{\gamma} \quad (\text{Langevin})$$

$$Q(q) = \frac{\omega_0(q)}{\gamma} \frac{1}{4\sin^2(qa/2)} \quad (\text{DPD}). \quad (25)$$

In the long wavelength limit where $q \rightarrow 0$, Langevin dynamics will always be overdamped, while DPD dynamics will be underdamped, provided that the system is not intrinsically overdamped as is the case in the vicinity of a continuous phase transition. Although these calculations have only been done for a linear harmonic chain, the results suggest that DPD has little effect on dynamical quantities that couple to long wavelengths. One of them would be the bulk viscosity of a system, although the estimation of DPD induced artifact in viscosity requires a different treatment than the one for sound waves [51]. Nevertheless, it was found that the measured bulk viscosity in sheared fluids depended on the precise choice of γ only in a negligible manner at least as long as γ was kept reasonably small [51].

In some cases, it may yet be beneficial to work with Langevin thermostats. The reason is that (elastic) long wavelength modes equilibrate notoriously slowly. Imagine we press an elastic solid onto a fractal surface. As the DPD thermostat barely damps long-range oscillations, we must expect a lot of bumping before the center-of-mass of the top wall finally comes to rest. Conversely, Langevin dynamics can lead to faster convergence because it couples

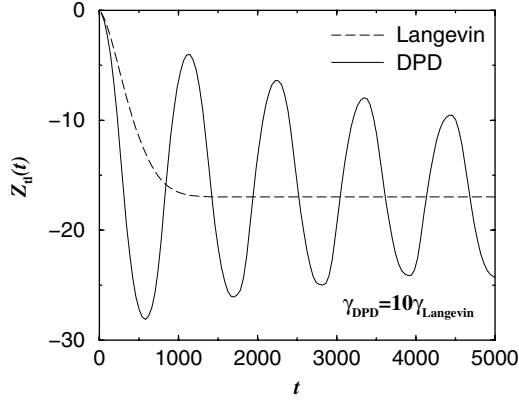


Fig. 10. Time dependence of the normal position Z_{t1} of an elastic solid, which is pressed against a self-affine substrate similar to the one shown in Fig. 7. Two different damping/thermostating schemes are employed, Langevin (*broken lines*) and DPD (*full lines*). Although the damping coefficient is 10 times greater in DPD than in Langevin, DPD-based dynamics are too strongly underdamped to relax efficiently to the right position

more strongly to long-wavelength oscillations. Figure 10 confirms this expectation. The Langevin-thermostatted system quickly reaches its mechanical position, while the DPD-thermostatted system is strongly underdamped, although the damping coefficient was 10 times larger for DPD than for Langevin.

In general, one needs to keep in mind that equilibrating quickly and producing realistic dynamics (or calculating thermal expectation values) are often mutually exclusive in simulations. It is necessary to consider carefully which aspect is more important for a given question of interest.

3.4 Determination of Bulk Viscosities

Theoretical Background: Role of Length Scales

In some cases friction between two surfaces is dominated by the bulk viscosity of the fluid embedded between the two surfaces [58]. When the surfaces are sufficiently far from one another and shear rates are low, one can usually assume that the velocity of the fluid near solid surfaces is close to the velocity of those surfaces. This scenario would be called a stick condition. As the distance, D , between the surfaces is decreased, one might have partial slip as alluded to in Fig. 6, in which the slip length, Λ , is introduced. The calculation of Λ from atomistic simulations is a subtle issue, [59] which we will not touch further upon here. When the fluid is confined even further, the concept of slip length might break down altogether and the measured friction becomes a true system function, which cannot be subdivided into smaller, independent entities. The discussion is summarized in the following equation

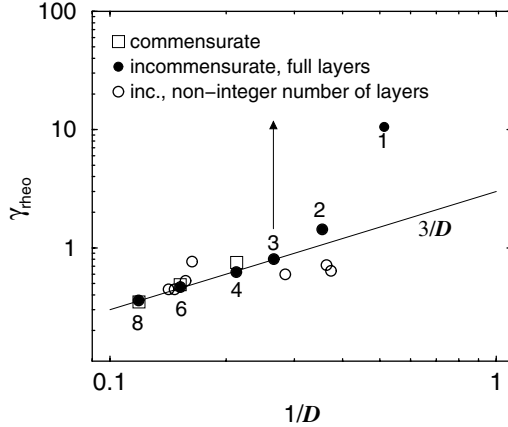


Fig. 11. Damping coefficient $\gamma_{rheo} = F/Av$ obtained from simulating two atomically flat surfaces separated by a simple fluid consisting of monomers at constant temperature and normal pressure. Different coverages were investigated. The numbers in the graph denote the ratio of atoms contained in the fluid N_{fl} relative to the atoms contained per surface layer of one of the two confining walls N_w . The walls are [111] surfaces of face-centered-cubic solids. They are rotated by 90° with respect to each other in the incommensurate cases. Full circles represent data for which N_{fl}/N_w is an integer. The arrow indicates the point at which the damping coefficients for commensurate walls increases exponentially

$$F/A = \begin{cases} \eta v/D & \text{hydrodynamic regime} \\ \eta v/(D + \Lambda) & \text{moderate confinement} \\ ? & \text{strong confinement} \end{cases}, \quad (26)$$

where F/A is the force, F , per surface area, A , required to slide two solids separated by a distance, D , at a velocity, v . η denotes the (linear-response) viscosity of the fluid between the walls. Figure 11 illustrates this point further. Shown is the linear response of a system similar to the one in the inset of Fig. 4. At large separations, the behaviour is reminiscent of hydrodynamic lubrication, i.e., the damping coefficient, $\gamma_{rheo} = F/Av$, is approximately inversely proportional to D . As D is decreased, the shear response is starting to become very sensitive to the relative orientation of the two surfaces. In fact, the damping force for commensurate surfaces increases by several orders of magnitude by going from 4 layers to 3 layers of lubricant atoms. The large values for the effective damping can be understood from the discussion of lubricated commensurate surfaces in Sect. 2.4. Keep in mind that the finite size of the walls prevents the energy barrier to become infinitely large for the commensurate walls. This is the reason why damping remains finite. Incommensurate walls do not show such size effects.

For a more detailed discussion of flow boundary conditions we refer to [2]. Here, it shall only be said that the two key ingredients from a microscopic

point of view are adhesion and the roughness of the walls. Perfectly flat walls will produce a perfect slip condition, while rough walls favor stick conditions. Increasing adhesion will also favor stick conditions at fixed roughness.

Lees-Edwards Boundary Conditions

In the hydrodynamic regime, it is unnecessary to impose shear via moving walls. It is often desirable to shear the fluid without any boundary effects. This can be achieved with the help of Lees-Edwards periodic boundary conditions, [60] which are illustrated in Fig. 12. Periodic boundary conditions are employed in all three spatial directions. However, while the center-of-mass of the central simulation cell remains fixed in space, many of its periodic images are moved parallel to the shear direction. As a consequence, even when a particle is fixed with respect to the central image, the distance to its periodically-repeated images will change with time if the vector connecting the two images contains a component parallel to the shear gradient direction.

To be specific, let \mathbf{R}_{ij} denote the position in the periodically repeated cell which is the i 's image to the right and the j 's image on top of the central cell. (A potentially third dimension remains unaffected and will therefore not be mentioned in the following.) The position in real space of the vector $\mathbf{R}_{ij} = (X, Y)_{ij}$ would be

$$\begin{pmatrix} X \\ Y \end{pmatrix}_{ij} = \begin{pmatrix} X \\ Y \end{pmatrix}_{00} + \begin{bmatrix} 1 & \dot{\epsilon} t \\ 0 & 1 \end{bmatrix} \begin{pmatrix} iL_x \\ jL_y \end{pmatrix}, \quad (27)$$

$\dot{\epsilon}$ being the shear rate, and L_x and L_y being the length of the simulation cell in x and y direction, respectively. Thus, conventional periodic boundary

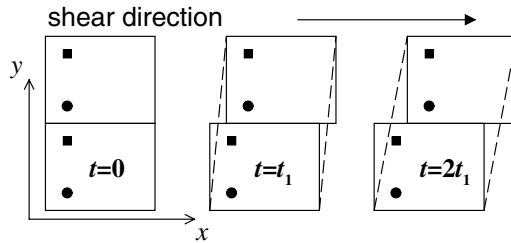


Fig. 12. Visualizations of Lees-Edwards periodic boundary conditions. At time zero, $t = 0$, regular periodic boundary conditions are employed. As time moves on, the periodic images of the central simulation cell move relative to the central cell in the shear direction as shown in the middle and the right graph. *Circle* and *square* show points in space that are fixed with respect to the (central) simulation cell. It is important to distribute the effect of shear homogeneously through the simulation cell such as indicated by the dashed lines. Otherwise, velocities will be discontinuous in shear direction whenever a particle crosses the simulation cell's boundary across the shear gradient direction. In this graph, x corresponds to the shear direction and y to the shear gradient direction

conditions can be reproduced by setting $\dot{\epsilon}$ to 0. When using Lees-Edwards periodic boundary condition, thermostating is most naturally done with DPD thermostats, because no reference system needs to be defined.

When integrating the equations of motion, it is important to not only impose the shear at the boundaries, because this would break translational invariance. Instead, in each MD step of size Δt , we need to correct the position in shear direction. This is done, for instance, in the following fashion:

$$X_{n+1} = X_n + \Delta X_n + \dot{\epsilon} \Delta t Y_n, \quad (28)$$

where ΔX_n is the change in the y coordinate if no external shear were applied. This way, the effect of shear is more homogeneously distributed over the simulation.

A better alternative to the implementation of Lees-Edwards boundary conditions is the formalism put forth by Parrinello and Rahman for the simulation of solids under constant stress [61]. They described the positions of particles by reduced, dimensionless coordinates r_α , where the r_α can take the value $0 \leq r_\alpha < 1$ in the central image. Periodic images of a particle are generated by adding or subtracting integers from the individual components of \mathbf{r} .

The real coordinates of \mathbf{R} are obtained by multiplying \mathbf{r} with the matrix h that contains the vector spanning the simulation cell. In the present example, this would read

$$R_\alpha = \sum_{\beta} h_{\alpha\beta} r_\beta \quad (29)$$

$$h = \begin{bmatrix} L_x & 0 \\ 0 & L_y \end{bmatrix} \begin{bmatrix} 1 & \dot{\epsilon} t \\ 0 & 1 \end{bmatrix}. \quad (30)$$

The potential energy, V , is now a function of the reduced coordinates and the h -matrix. For the kinetic energy, one would only be interested in the motion of the particle relative to the distorted geometry so that a suitable Lagrange function, L_0 , for the system would read

$$L_0 = \sum_i \frac{1}{2} m_i \left(\sum_{\beta} h_{\alpha\beta} \dot{r}_{i\beta} \right)^2 - V(h, \{\mathbf{r}\}), \quad (31)$$

in which the h matrix may be time dependent. From this Lagrangian, it is straightforward to derive the Newtonian equations for the reduced coordinates, which can then be solved according to the preferred integration schemes. One advantage of the scheme outlined in (29)–(31) is that it is relatively easy to allow for fluctuations of the size of the central cell. This is described further below.

Geometric and Topological Constraints

Note that L_x and L_y can be chosen to be time dependent. When simulating simple fluids under shear, there is no particular reason why they should be

chosen independent from one another. However, when simulating self-assembled monolayers under shear, which have received significant attention due to their technological applications, it may be necessary to allow independent fluctuations of the cell geometry along different spatial dimensions. This will be discussed in the context of diblock copolymers.

The most simple diblock copolymers are linear molecules, in which one part of the chain consists of one type of monomer, say polystyrene (PS), and the other one of another type, say polybutadiene (PB), see Fig. 13. PS and PB usually phase separate at low temperatures, however, due to their chemical connectivity, blockcopolymers cannot unmix on a macroscopic scale. They can only phase separate on a microscopic scale, whose size is determined by the length of the polymers.

When lamellar structures are formed, it is necessary to choose the dimension of the simulation cell commensurate with the intrinsic periodicity of the lamellae, in order to avoid any pressure that is unintentionally exerted due to geometric constraints. It is therefore desirable to allow the system to fluctuate parallel to “solid directions,” which are introduced in Fig. 13. For these directions, it would be appropriate to employ the usual techniques related to constant stress simulations [61].

Let us consider the three-dimensional case and further work within the Parrinello-Rahman framework. A rather general three-dimensional h matrix will be considered

$$h = \begin{bmatrix} L_{xx} & 0 & L_{xz} \\ 0 & L_{yy} & L_{yz} \\ L_{xz} & L_{yz} & L_{zz} \end{bmatrix} \begin{bmatrix} 1 & \dot{\epsilon} t & 0 \\ 0 & 1 & 0 \\ 0 & 0 & 1 \end{bmatrix}. \quad (32)$$

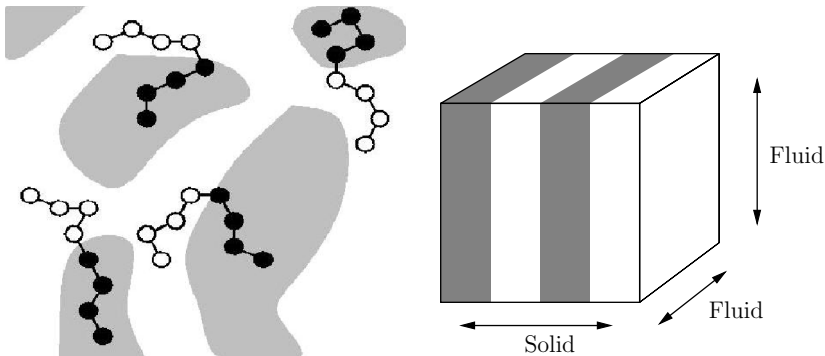


Fig. 13. Schematic representation of the microphase separation of block copolymers. The *left* graph shows atomic-scale details of the phase separation at intermediate temperatures, the *right* graph a lamellar phase formed by block copolymers at low temperatures. The block copolymers have solid-like properties normal to the lamellae, due to a well-defined periodicity. In the other two directions, the system is isotropic and has fluid-like characteristics. From [62]

It is now possible to treat the variables $L_{\alpha\beta}$ as generalized coordinates and allow them to adjust within the MD simulation. For this purpose, it is necessary to define a kinetic energy T_{cell} associated with the fluctuation of the cell geometry as a bilinear function of generalized velocities $\dot{L}_{\alpha\beta}$,

$$T_{\text{cell}} = \sum_{\alpha\beta\gamma\delta} \frac{1}{2} M_{\alpha\beta\gamma\delta} \dot{L}_{\alpha\beta} \dot{L}_{\gamma\delta}, \quad (33)$$

where $M_{\alpha\beta\gamma\delta}$ must be a positive definite matrix with the unit of mass. Though the optimum choice for the M -matrix is a matter of discussion, [63] a reasonable approach is to treat the various $\dot{L}_{\alpha\beta}$ as independent, uncoupled variables and to assign the same mass M_{cell} to all diagonal elements, $M_{\alpha\beta\alpha\beta}$ which simplifies (33) to

$$T_{\text{cell}} = \sum_{\alpha,\beta\leq\alpha} \frac{1}{2} M_{\text{cell}} \dot{L}_{\alpha\beta}^2. \quad (34)$$

It is often sensible to choose M_{cell} such that the simulation cell adjusts on microscopic time scales to the external pressure.

The Lagrange function L for Lees-Edwards boundary conditions combined with Parrinello Rahman fluctuations for the cell geometry now reads

$$L = L_0 + T_{\text{cell}} - p \det h, \quad (35)$$

where p is an isotropic pressure and $\det h$ the volume of the simulation cell. The Newtonian equations of motion for the generalized coordinates $L_{\alpha\beta}$ and \mathbf{r}_i follow from the Lagrange formalism. Furthermore, it is possible to couple fluctuating cell geometries not only to constant isotropic pressure but also to non-isotropic stresses. The description of these approaches is beyond the scope of the present manuscript, but they can be found in the literature [61].

When studying systems with mixed “fluid” and “solid” directions, it is important to keep in mind that each solid direction should be allowed to breathe and fluid directions need to be scaled isotropically or to be constrained to a constant value. Allowing two fluid directions to fluctuate independently from one another allows the simulation cell to become flat like a pancake, which we certainly would like to avoid. To give an example, consider Fig. 14, in which a lamellar block copolymer phase is sheared. The convention would be to have the shear direction parallel to x and the shear gradient direction parallel to y . There is no reason for the simulation cell to distort such that $L_{xz} = L_{yz} = 0$ would not be satisfied on average, so one may fix the values of L_{xz} and L_{yz} from the beginning. There is one solid direction plus two fluid directions. We can also constrain L_{xx} to a constant value, because the shear direction will always be fluid and there is another fluid direction that can fluctuate. This means that we should allow the simulation cell to fluctuate independently in the shear and the shear gradient direction. Yet during the reorientation process, i.e., during the intermediate stage shown in Fig. 14,

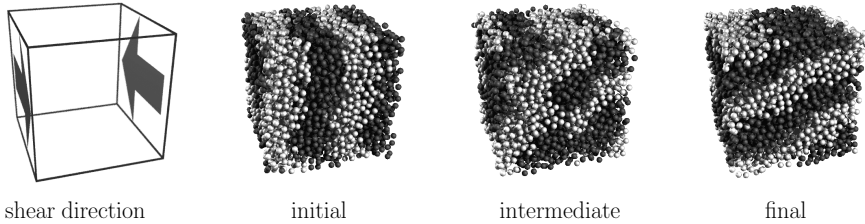


Fig. 14. A lamellar block copolymer phase is reoriented through external shear. The initial phase has the director of the lamellae parallel to the shear gradient direction. The most stable state would be to orient the director parallel to the shear and shear gradient direction. However, the reorientation process gets stuck before true equilibrium is reached. The stuck orientation is relatively stable, because the lamellae have to be broken up before they can further align with respect to the shear flow. From [64]

simulation cells do have the tendency to flatten out, because periodicity and hence solid like behaviour is lost for a brief moment in time.

It is interesting to note that the reorientation process of the lamellae does not find the true equilibrium state but gets stuck in a metastable state. The periodic boundary conditions impose a topological constraint and prevent the system from simply reorienting. It is conceivable that similar metastable states are also obtained experimentally, although the nature of the constraints differs in both cases. One means of overcoming this topological constraint is to impose a higher temperature, T_h , at the boundaries of the simulation cell (e.g. at $0 \leq r_y \leq 0.2$ and $0 \leq r_z \leq 0.2$) and to keep the temperature low in the remaining system [62]. This would melt the lamellar structure at the boundary and allow the remaining lamellae to reorient freely with respect to the shear flow.

4 Selected Case Studies

The last few years have seen an increasing number of tribological simulations that incorporate realistic potentials and/or realistic boundary conditions. Unfortunately, it is not possible in this chapter to give all of these studies the exposure that they may deserve. Instead, two subjects will be selected. One deals with the occurrence and breakdown of superlubricity. The other subject evolves around the chemical complexity of real lubricant mixture and ways how simulations can aid in the rational design of lubricant mixtures.

4.1 Superlubricity and the Role of Roughness at the Nanometer Scale

In Sect. 2, it is argued that two three-dimensional solids with clean, flat surfaces should be superlubric, unless conditions are extreme. Calculations of

Hirano and Shinjo, in particular, supported this picture at an early stage for three-dimensional solids and realistic model potentials [4, 5]. Theoretical considerations, moreover, predict that low-dimensional systems are less likely to be superlubric because they are more easily deformed on large length scales than highly-dimensional structures [9]. But, even for one-dimensional Frenkel Kontorova (FK) chains, the interaction between chain and substrate has to be sufficiently strong, in order to produce finite kinetic friction [34]. Reasonable parametrizations of the FK model would require the harmonic coupling between adjacent atoms in the chain, k , to be larger than the maximum curvature, V''_{\max} , of the embedding potential [9]. In this regime, FK models are typically superlubric [34]. Thus, all theoretical considerations point to superlubricity between unaligned solids, provided that the interfaces are sufficiently flat. While more and more systems are found to be superlubric, some experiments find clear violations of superlubricity, although theory predicts these same systems to be superlubric. One example, is the measurement of friction anisotropy at Ni(100)/Ni(100) interfaces in ultra high vacuum [65]. When misoriented by 45° , friction coefficients remained in the order of 2.5 instead of becoming unmeasurably small. The simulations by Tangney et al. [66] and by Qi et al. [67] probably clarify the seeming discrepancy between theory and simulation.

Tangney et al. [66] studied the friction between an inner and an outer carbon nanotube. Realistic potentials were used for the interactions within each nanotube and Lennard Jones potentials were employed to model the dispersive interactions between nanotubes. The intra-tube interaction potentials were varied and for some purposes even increased by a factor of 10 beyond realistic parametrizations, thus artificially favoring the onset of instabilities and friction. Two geometries were studied, one in which inner and outer tubes were commensurate and one in which they were incommensurate.

Let us rewind for a second to discuss the two idealized egg cartons mentioned in the beginning of Sect. 2.4. Aligning the two egg cartons explains static friction, but, as long as no additional “microscopic” dissipation mechanism is present, there is no reason why our egg cartons should show static friction. Whenever the top egg carton slides downwards, kinetic energy is produced that will help it to climb up the next potential energy maximum. Instabilities would be required to produce static friction. Thus, the presence of static friction does not imply kinetic friction. The simulations of the nanotubes exhibit exactly this behaviour, which is demonstrated in Fig. 15.

In interpreting Fig. 15, it is important to know that the outer tube has two open endings and that both tubes are equally long. The embedded tube only has a small fraction inside the outer tube initially. The system will try to reduce surface energy by sucking the outer tube inside the inner tube. If there is no friction between the tubes, then the force will be constant until the inner tube starts to exit at the other end at high velocity. When the nanotube is almost completely exited at the other end, the procedure will repeat and surface-energy driven oscillations will occur. This is what is found

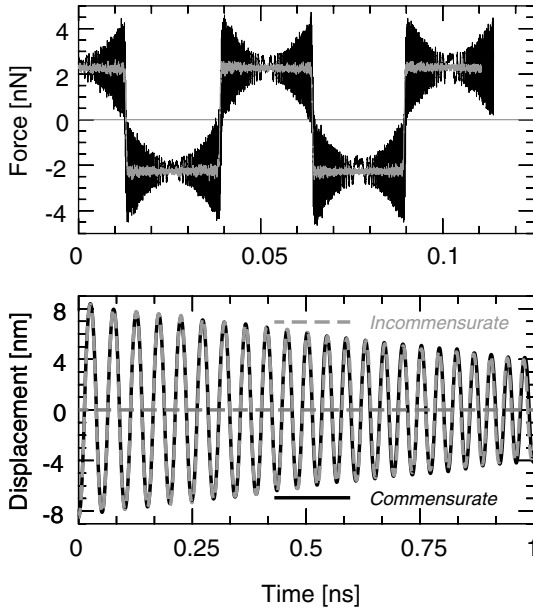


Fig. 15. *Top:* Friction force between two nanotubes as a function of time. *Bottom:* Displacement of the nanotubes as a function of time. Grey and black lines indicate incommensurate and commensurate geometries, respectively. From [66]

for the incommensurate tube, except for some small fluctuations in the instantaneous force and some weak viscous-type damping. The commensurate system behaves slightly different. There are large fluctuations in the instantaneous force, which have the periodicity of the lattice. The fluctuations are particularly large when the inner tube is fully immersed in the outer one. The fluctuations can be understood within the egg carton model. Moreover, from the absence of significant dissipation on long time scales, it is possible to conclude that no instabilities occur. Thus the simulated, low-dimensional rubbing system exhibits superlubricity, not only for incommensurate but even for commensurate surfaces. Finite static and zero kinetic friction forces have also been observed experimentally, albeit for a different system [68]. Although the nanotube simulations were based on reasonably realistic potentials, it needs to be emphasized that real carbon nanotubes have a lot of chemical defects, which induce the experimentally measured non-viscous type friction forces [69].

It turns out that the detailed microstructure matters just as much for three-dimensional systems as for nanotubes. Qi et al. [67] studied atomically smooth Ni(100)/Ni(100) interfaces. Their idealized geometries display the same superlubric behaviour as the idealized copper interfaces studied by Hirano and Shinjo [4]. However, roughening the top layer with a mere 0.8 \AA rms variation, changes the behaviour completely, with friction coefficients increasing by several orders of magnitude as can be seen in Fig. 16.

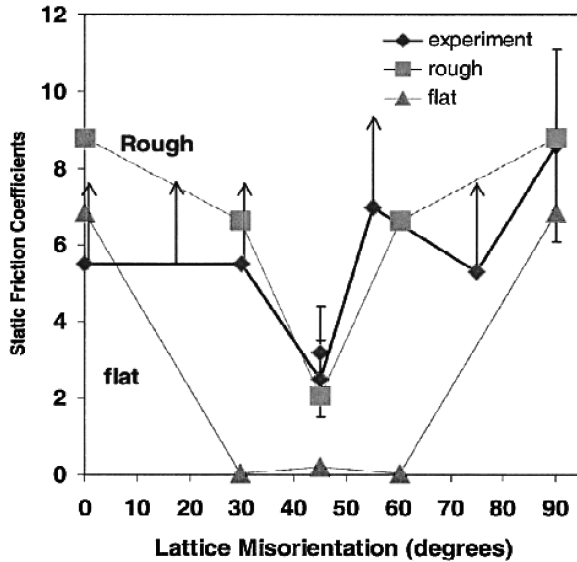


Fig. 16. Friction coefficient for differently aligned Ni(100)/Ni(100) interfaces. Rough surfaces have a 0.8 Å rms variation in roughness added to the atomically smooth surfaces. From [67]

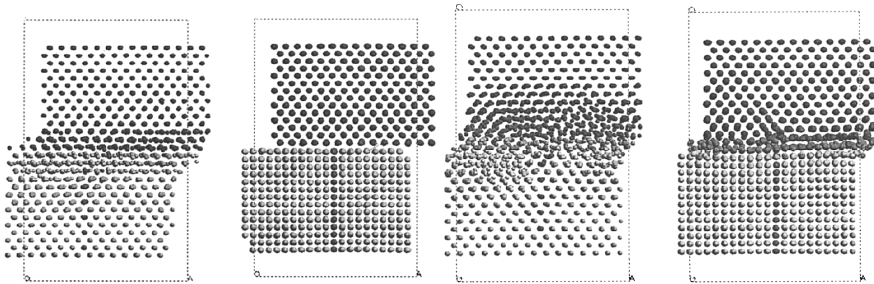


Fig. 17. Snapshots from the simulations leading to the friction coefficients shown in Fig. 16. From the left to the right: Atommically flat commensurate, atommically flat incommensurate, rough commensurate, and rough incommensurate geometries. Only the flat incommensurate surfaces remain undamaged resulting in abnormally small friction coefficients. From [67]

The microscopic origin of the increase in friction can be understood from the microstructures shown in Fig. 17. Due to sliding, all contacts deform plastically except for the atommically flat, incommensurate contact. As the atoms are no longer elastically coupled to their lattice sites, they can interlock the surfaces in a way that is roughly akin of the scenario shown in Fig. 2. Of course, when placing two commensurate, atommically smooth solids on top of each other, the identity of each of the solids disappears instantaneously, and

sliding them corresponds to shearing a single crystal, which certainly has finite resistance to shear. No intervening layer is required in this case to interlock the surfaces.

4.2 Physics and Chemistry of Lubricant Additives

Most of this chapter evolves around simple models of surfaces and lubricants. There is a lot we can learn from these generic models, but it is important to keep in mind that real lubricants are rather complex mixtures. There are many different chemicals which are added to the so-called base oil of industrial lubricants used in car engines. These additives function to reduce the formation of foam, to reduce friction, to disperse debris, to act as anti-oxidants for nascent surface material, and to reduce wear. The rational formulation of an industrial lubricant formulation not only requires a knowledge of each additive, but it is also imperative to understand the interactions between the additives.

One particular class of anti-wear additives are zinc dialkyldithiophosphates (ZDDPs), which were invented in the 1930's as anti-oxidants. Their main function, however, turned out to be the protection of cast iron surfaces from wear. Experiments revealed that the ZDDPs decompose into simple zinc phosphates (ZPs) under the conditions at which the lubricant operates and that these decomposition products form films or patches of ZPs on surfaces. In what follows, these patches will be called anti-wear pads (AWP). Although an abundance of experimental data was available regarding the ZDDPs, no coherent, molecular theory existed that could explain how the AWP's form and function [70]. Relevant experimental observations which must be accounted for by such a theory include the following: AWP's formed on the tops of asperities are harder and more elastic than those in the valleys between asperities, the spectra of the AWP's on the tops of asperities are reminiscent of ZPs with longer chain lengths, while those in the valleys are characteristic of shorter ZP chains. Additionally, the ability of the AWP's to inhibit wear is reduced when zinc is replaced by another charge-balancing cation, such as calcium. Lastly, the rapid formation of AWP's under sliding conditions and the inability of ZDDPs to protect aluminum surfaces were not understood.

Previous models for ZP-AWP formation were based on reaction schemes in which iron atoms acted catalytically in the formation of the pads. It was believed that the reaction required the high temperatures typically found in the microscopic points of contact. However, the conditions found in tribological contacts are far from ambient and it may therefore not be sufficient to only incorporate the effect of temperature. In contrast, pressures can be extremely high, and approach the theoretical yield pressure for a short period of time. With these considerations in mind, it is natural to ask, how the lubricant molecules respond to the extreme conditions encountered in tribological contacts.

Mosey et al. [71] addressed this question by exposing the relevant decomposition products of ZDDPs to pressures close to the theoretical yield strengths of steel and aluminium, respectively. Configurations from these simulations before, during, and after compression are shown in Fig. 18. It is found that

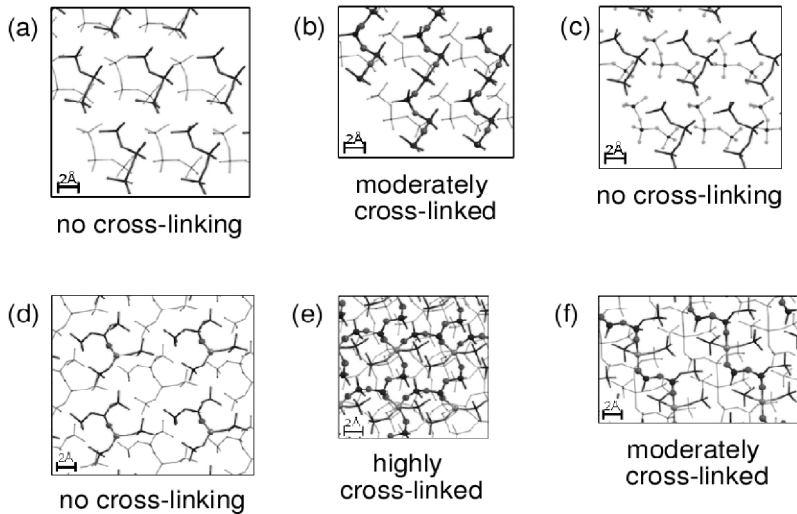


Fig. 18. Molecular configuration of triphosphates (TPs) (a)–(c) and zinc phosphates (ZPs) (d)–(f). The graphs (a) and (d) correspond to an initial low-pressure structure. The graphs (b) and (e) show configurations at high pressure, in which both TPs and ZPs form covalent cross links. After pressure is released back to ambient pressures, (c) and (f), only the ZPs remain a chemically connected network

high pressure is a sufficient condition to form chemically connected networks. However, these networks only remain intact under decompression if zinc is present as a crosslink-forming agent. The formation of the cross-links occurs through changes in the coordination at the zinc atom. Since calcium does not exhibit a variable coordination, replacing zinc with that atom decreases the degree to which cross-linking occurs, thereby reducing the ability of the film to inhibit wear. From the simulations one may conclude that the degree of chemical connectivity is particularly large, when the pressure to which the ZPs are exposed are very high. Moreover, it was found that the chemically cross-linked ZPs are much harder after the compression than before. Lastly, the formed pads are harder than aluminium surfaces suggesting that they cannot effectively redistribute pressures on aluminium surfaces and instead abrade them. All these conclusions are in correspondance to the experimental observations.

More importantly, the simulations provide guidelines with which to screen for replacements of the environmentally problematic ZDDPs. One needs to identify molecules that can enter the microscopic points of contact as a

viscous fluid and that crosslink through the application of the typically encountered pressure and temperature conditions. (Temperature appeared to play a negligible role in the simulations.) The resulting cross-linked AWP should be softer, but not much softer, than the substrate so that the AWP can redistribute the pressure exerted and thereby alleviate the extreme conditions to which the asperities are exposed. This example is only one of many which show that simulations bear the potential to not only address questions of fundamental scientific interest, but also guide in the design of new materials.

Acknowledgments

Financial support from the Natural Sciences and Engineering Research Council of Canada and SHARCnet (Ontario) is gratefully acknowledged. The author thanks Carlos Campana for providing Figs. 7 and 10 and Nick Mosey for providing Fig. 18. The authors also acknowledges helpful discussions with Carlos Campana and Nick Mosey.

References

1. J. A. Harrison, S. J. Stuart, and D. W. Brenner (1999) Atomic-scale simulation of tribological and related phenomena. In *Handbook of Micro/Nanotribology* Ed. B. Bhushan (CRC Press, Boca Raton, FL), pp. 525–594
2. M. O. Robbins and M. H. Müser (2001) Computer simulations of friction, lubrication, and wear. In *Modern Tribology Handbook* Ed. B. Bhushan (CRC Press, Boca Raton, FL), pp. 717–765 (cond-mat/0001056)
3. M. H. Müser, M. Urbakh, and M. O. Robbins (2003) Statistical mechanics of static and low-velocity kinetic friction. *Adv. Chem. Phys.* **126**, pp. 187–272
4. M. Hirano and K. Shinjo (1990) Atomistic locking and friction. *Phys. Rev. B* **41**, pp. 11837–11851
5. K. Shinjo and M. Hirano (1993) Dynamics of friction - superlubric state *Surf. Sci.* **283**, pp. 473–478
6. L. Prandtl (1928) Ein Gedankenmodell zur kinetischen Theorie der festen Körper. *Z. Angew. Math. Mech.* **8**, pp. 85–106
7. G. A. Tomlinson (1929) A molecular theory of friction. *Philos. Mag. Series 7*, pp. 905–939
8. T. Baumberger and C. Caroli (1990) Dry friction dynamics at low velocities. *Comments Cond. Mater. Phys.* **62**, p. 251
9. M. H. Müser (2004) Structural lubricity: Role of dimension and symmetry. *Europhys. Lett.* **66**, pp. 97–103
10. B. N. J. Persson (2001) Theory of rubber friction and contact mechanics. *J. Chem. Phys.* **115**, pp. 3840–3861
11. F. P. Bowden and D. Tabor (1986) *The Friction and Lubrication of Solids*. Clarendon Press, Oxford
12. S. Hyun, L. Pei, J.-F. Molinari, and M. O. Robbins (2004) Finite-element analysis of contact between elastic self-affine surfaces. *Phys. Rev. E* **70**, p. 026117

13. G. He, M. H. Müser, and M. O. Robbins (1999) Adsorbed layers and the origin of static friction. *Science* **284**, pp. 1650–1652
14. M. H. Müser, L. Wenning, and M. O. Robbins (2001) Simple microscopic theory of Amontons' laws for static friction. *Phys. Rev. Lett.* **86** pp. 1295–1298
15. J. N. Glosli and G. McClelland (1993) Molecular dynamics study of sliding friction of ordered organic monolayers. *Phys. Rev. Lett.* **70**, pp. 1960–1963
16. H. A. Harrison, C. T. White, R. J. Colton, and D. W. Brenner (1995) Investigation of the atomic-scale friction and energy-dissipation in diamond using molecular-dynamics. *Thin Solid Films* **260**, pp. 205–211
17. G. T. Gao, P. T. Mikulski, and J. A. Harrison (2002) Molecular-scale tribology of amorphous carbon coatings: Effects of film thickness, adhesion, and long-range interactions. *J. Am. Chem. Soc.* **124**, pp. 7202–7209
18. N. J. Mosey, T. K. Woo, and M. H. Müser (2005) Energy dissipation via quantum chemical hysteresis during high-pressure compression: A first-principles molecular dynamics study of phosphates. *Phys. Rev. B* **72**, p. 054124
19. D. Dowson (1979) *History of Tribology* Longman, New York
20. M. H. Müser (2002) Simple microscopic theory of Amontons's laws for static friction. *Phys. Rev. Lett.* **89**, p. 224301
21. Y. Sang, M. Dubé, and M. Grant (2001) Thermal effects on atomic friction. *Phys. Rev. Lett.* **87**, p. 174301
22. O. K. Dudko, A. E. Filippov, J. Klafter, and M. Urbakh (2002) Dynamic force spectroscopy: a Fokker-Planck approach. *Chem. Phys. Lett.* **352**, pp. 499–504
23. G. He and M. O. Robbins (2001) Simulations of the kinetic friction due to adsorbed surface layers. *Tribol. Lett.* **10**, pp. 7–14
24. J. H. Dieterich and B. D. Kilgore (1994) Direct observation of frictional contacts: New insights for state-dependent properties. *Pure Applied Geophys.* **143**, pp. 283–302
25. J. H. Dieterich and B. D. Kilgore (1996) Imaging surface contacts: power law contact distributions and contact stresses in quartz, calcite, glass and acrylic plastic. *Tectonophysics* **256**, pp. 219–239
26. G. He and M. O. Robbins (2001) Simulations of the static friction due to adsorbed molecules. *Phys. Rev. B* **64**, p. 035413
27. L. Wenning and M. H. Müser (2001) Friction laws for elastic nano-scale contacts. *Europhys. Lett.* **54**, pp. 693–699
28. A. W. Bush, R. D. Gibson, and T. R. Thomas (1975) The Elastic Contact of a Rough Surface. *Wear*, **35**, p. 87
29. B. N. J. Persson (2001) Elastoplastic contact between randomly rough surfaces. *Phys. Rev. Lett.* **87**, p. 116101
30. B. Q. Luan, S. Hyun, M. O. Robbins, and N. Bernstein (2005) Multiscale modeling of two dimensional rough surface contacts. *Mater. Res. Soc. Symp. Proc.* **841**, pp. R7.4.1–10
31. M. Schoen, C. L. Rhykerd, D. J. Diestler, and J. H. Cushman (1989) Shear forces in molecularly thin films. *Science* **245**, pp. 1223–1225
32. M. H. Müser and M. O. Robbins (2000) Conditions for static friction between flat crystalline surfaces. *Phys. Rev. B* **61**, pp. 2335–2342
33. E. Gnecco, R. Bennewitz, T. Gyalog, and E. Meyer (2001) Friction experiments on the nanometre scale. *J. Phys.: Condens. Mat.* **13**, pp. R619–R642
34. O. M. Braun and Y. S. Kivshar (1998) Nonlinear dynamics of the Frenkel-Kontorova model. *Phys. Repp.* **306**, pp. 2–108

35. J. E. Hammerberg, B. L. Holian, J. Roder, A. R. Bishop, and S. J. Zhou (1998) Nonlinear dynamics and the problem of slip at material interfaces. *Physica D* **123**, pp. 330–340
36. W. A. Steele (1973) The physical interaction of gases with crystalline solids. *Surf. Sci.* **36**, pp. 317–352
37. M. O. Robbins and P. A. Thompson (1991) Critical velocity of stick-slip motion. *Science* **253**, p. 916
38. B. Q. Luan and M. O. Robbins (2004) Effect of inertia and elasticity on stick-slip motion. *Phys. Rev. Lett.* **93**, p. 036105
39. V. Zaloj, M. Urbakh, and J. Klafter (1998) Atomic scale friction: What can be deduced from the response to a harmonic drive? *Phys. Rev. Lett.* **81**, pp. 1227–1230
40. P. Meakin (1998) *Fractals, Scaling and Growth far from Equilibrium*. Cambridge University Press, Cambridge
41. J. Q. Broughton, F. F. Abraham, N. Bernstein, and E. Kaxiras (1999) Concurrent coupling of length scales: Methodology and application. *Phys. Rev. B* **60**, pp. 2391–2403
42. W. A. Curtin and R. E. Miller (2003) Atomistic/continuum coupling in computational materials science. *Model. Simul. Mater. Sci.* **11**, pp. R33–R68
43. Y. Saito (2004) Elastic lattice Green's function in three dimensions. *J. Phys. Soc. Japan* **73**, p. 1816
44. W. Cai, M. de Koning, V. V. Bulatov, and S. Yip (2000) Minimizing boundary reflections in coupled-domain simulations. *Phys. Rev. Lett.* **85**, pp. 3213–3216
45. S. A. Adelman and J. D. Doll (1974) (a) Generalized Langevin equation approach for atom/solid-surface scattering: Collinear atom/harmonic chain model. (b) Erratum: Generalized Langevin equation approach for atom/solid-surface scattering: Collinear atom/harmonic chain model. (c) Generalized Langevin equation approach for atom/solid-surface scattering: General formulation for classical scattering off harmonic solids. *J. Chem. Phys.* **61**, pp. 4242–4245; *ibid.*, (1975) **62**, pp. 2518–2518; *ibid.*, (1976) **64**, pp. 2375–2388
46. R. Kubo (1966) The fluctuation-dissipation theorem. *Rep. Prog. Phys.* **29**, pp. 255–284
47. T. Schneider and E. Stoll (1978) Molecular-dynamics study of a three-dimensional one-component model for distortive phase transitions. *Phys. Rev. B* **17**, pp. 1302–1322
48. P. Español and P. Warren (1995) Statistical mechanics of dissipative particle dynamics. *Europhys. Lett.* **30**, pp. 191–196
49. S. S. Sarman, D. J. Evans, and P. T. Cummings (1998) Recent developments in non-Newtonian molecular dynamics. *Phys. Rep.* **305**, pp. 1–92
50. P. Español (1995) Hydrodynamics from dissipative particle dynamics. *Phys. Rev. E* **52**, pp. 1734–1742
51. T. Soddemann, B. Dünweg, and K. Kremer (2003) Dissipative particle dynamics: A useful thermostat for equilibrium and nonequilibrium molecular dynamics simulations. *Phys. Rev. E* **68**, p. 046702
52. A. Ricci and G. Ciccotti (2003) Algorithms for Brownian dynamics. *Mol. Phys.* **101**, pp. 1927–1931
53. D. J. Evans and G. P. Morriss (1990) *Statistical Mechanics of Nonequilibrium Liquids*. Academic Press, London; <http://rsc.anu.edu.au/evans/evansmorrissbook.htm>

54. D. J. Evans and G. P. Morriss (1986) Shear thickening and turbulence in simple fluids. *Phys. Rev. Lett.* **56**, pp. 2172–2175
55. W. Loose and G. Ciccotti (1992) Temperature and temperature control in nonequilibrium-molecular-dynamics simulations of the shear-flow of dense liquids. *Phys. Rev. A* **45**, pp. 3859–3866
56. M. J. Stevens and M. O. Robbins (1993) Simulations of shear-induced melting and ordering. *Phys. Rev. E* **48**, pp. 3778–3792
57. P. Reimann and M. Evstigneev (2004) Nonmonotonic velocity dependence of atomic friction. *Phys. Rev. Lett.* **93**, p. 230802
58. D. Dowson and G. R. Higginson (1968) *Elastohydrodynamic Lubrication*. Pergamon, Oxford
59. L. Bocquet and J.-L. Barrat (1993) Hydrodynamic boundary-conditions and correlation-functions of confined fluids. *Phys. Rev. Lett.* **70**, pp. 2726–2729
60. A. W. Lees and S. F. Edwards (1972) The computer study of transport processes under extreme conditions. *J. Phys. C* **5**, pp. 1921–1928
61. M. Parrinello and A. Rahman (1981) (a) Polymorphic transitions in single-crystals – a new molecular-dynamics method. (b) Strain fluctuations and elastic-constants. *J. Appl. Phys.* **52**, p. 7182; *ibid.* (1982); *J. Chem. Phys.* **76**, p. 2662
62. B. Fraser, M. H. Müser, and C. Denniston (2005) Diffusion, elasticity, and shear flow in self-assembled block copolymers: A molecular dynamics study. *J. Pol. Sci. B* **43**, pp. 969–981
63. R. M. Wentzcovitch (1991) Invariant molecular-dynamics approach to structural phase-transitions. *Phys. Rev. B* **44**, pp. 2358–2361
64. B. Fraser (2005) *Ph.D. thesis*. University of Western Ontario
65. J. S. Ko and A. J. Gellman (2000) Friction anisotropy at Ni(100)/Ni(100) interfaces. *Langmuir* **16**, pp. 8343–8351
66. P. Tangney, S. G. Louie, and M. L. Cohen (2004) Dynamic sliding friction between concentric carbon nanotubes. *Phys. Rev. Lett.* **93**, 065503
67. Y. Qi, Y.-T. Cheng, T. Caglan, and W. A. Goddard III (2002) Friction anisotropy at Ni(100)/(100) interfaces: Molecular dynamics studies. *Phys. Rev. B* **66**, 085420
68. A. Socoliuc, R. Bennewitz, E. Gneco, and E. Meyer (2004) Transition from stick-slip to continuous sliding in atomic friction: Entering a new regime of ultralow friction. *Phys. Rev. Lett.* **92**, p. 134301
69. Z. Xia and W. A. Curtin (2004) Pullout forces and friction in multiwall carbon nanotubes. *Phys. Rev. B* **69**, p. 233408
70. M. A. Nicholls, T. Do, P. R. Norton, M. Kasrai, and G. M. Bancroft (2005) Review of the lubrication of metallic surfaces by zinc dialkyl-dithiophosphates. *Tribol. Int.* **38**, pp. 15–39
71. N. J. Mosey, M. H. Müser, and T. K. Woo (2005) Molecular mechanisms for the functionality of lubricant additives. *Science* **307**, pp. 1612–1615